HHS Public Access

Author manuscript

Cancer Immunol Res. Author manuscript; available in PMC 2023 July 01.

Published in final edited form as:

Cancer Immunol Res. 2022 September 01; 10(9): 1141–1154. doi:10.1158/2326-6066.CIR-22-0110.

Sensory nerves impede the formation of tertiary lymphoid structures and development of protective anti-melanoma immune responses

Kavita Vats[1,a], **Oleg Kruglov**[1,a], **Bikram Sahoo**[2], **Vishal Soman**[3], **Jiying Zhang**[1], **Galina V. Shurin**[4], **Uma R. Chandran**[3], **Pavel Skums**[2], **Michael R. Shurin**[4,5,6], **Alex Zelikovsky**[2], **Walter J. Storkus**[1,5,6], **Yuri L. Bunimovich**[1,6,*]

[1]Department of Dermatology, University of Pittsburgh School of Medicine, Pittsburgh, PA, USA

[2]Department of Computer Science, Georgia State University, Atlanta, GA, USA.

[3]Department of Biomedical Informatics, University of Pittsburgh School of Medicine, PA, USA.

[4]Department of Pathology, University of Pittsburgh School of Medicine, Pittsburgh, PA, USA

[5]Department of Immunology, University of Pittsburgh School of Medicine, Pittsburgh, PA

[6]UPMC Hillman Cancer Center, Pittsburgh, PA 15213

Abstract

Peripheral neurons comprise a critical component of the tumor microenvironment (TME). The role of the autonomic innervation in cancer has been firmly established. However, the effect of the afferent (sensory) neurons on tumor progression remains unclear. Utilizing surgical and chemical skin sensory denervation methods, we showed that afferent neurons supported the growth of melanoma tumors *in vivo* and demonstrated that sensory innervation limited the activation of effective anti-tumor immune responses. Specifically, sensory ablation led to improved leukocyte recruitment into tumors, with decreased presence of lymphoid and myeloid immunosuppressive cells and increased activation of T-effector cells within the TME. Cutaneous sensory nerves hindered maturation of intratumoral high endothelial venules (HEVs) and limited formation of mature tertiary lymphoid-like structures containing organized clusters of $CD4^+$ T cells and B cells. Denervation further increased T-cell clonality and expanded the B-cell repertoire in the TME. Importantly, CD8a depletion prevented denervation-dependent anti-tumor effects. Finally, we observed that gene signatures of inflammation and the content of neuron-associated transcripts inversely correlated in human primary cutaneous melanomas, with the latter representing a negative prognostic marker of patient overall survival. Our results suggest that tumor-associated sensory neurons negatively regulate the development of protective anti-tumor immune responses

[*]Corresponding author: Yuri L. Bunimovich, MD, PhD, Department of Dermatology, University of Pittsburgh Medical Center, E1157 Thomas E. Starzl Biomedical Science Tower, 200 Lothrop Street, Pittsburgh, PA, 15213, (412)648-9983, bunimovichyl@upmc.edu.

Authors' contributions: KV, OK, YLB designed experiments. KV, OK, BS, VS, GVS, MRS, and YLB performed experiments. KV, OK, BS, VS, URC, GVS, PS, MRS, AZ, WJS, and YLB interpreted data. KV, OK, BS, VS, WJS, and YLB wrote the paper. All authors read and agreed on the final version of the submitted manuscript.

[a]KV and OK contributed equally to this work.

Conflict of interest: The authors declare no conflict of interest.

within the TME, thereby defining a novel target for therapeutic intervention in the melanoma setting.

Synopsis:

Sensory neurons are shown to play a critical role in the modulation of anti-tumor immune responses and the formation of tertiary lymphoid structures in melanoma. Data highlight afferent innervation as a potential novel target for cancer immunotherapy.

Keywords

Sensory nerve; melanoma; cancer; neuroimmunology; tumor microenvironment; tertiary lymphoid structure

INTRODUCTION

The tumor microenvironment (TME) exerts significant influence over the development and progression of cancer. Over the last decade, the peripheral nervous system (PNS) has been firmly established as a critical component of the TME, where it influences tumor initiation and growth, metastasis, and cancer-related pain [1]. Because the majority of past studies have focused on the autonomic nervous system, the role of sensory nerves (SNs) in cancer progression remains comparatively less understood. It is now generally accepted that adrenergic innervation promotes cancer progression. Adrenergic nerve density increases during prostate cancer development and correlates with more aggressive disease in breast, colorectal, lung, and prostate cancer models [2–6]. Sensory axonogenesis occurs in head and neck carcinoma and cervical cancer; however, it remains unclear whether all solid tumors exhibit sensory innervation [7–10]. Several studies utilizing sensory denervation have demonstrated the pro-tumor impact of SNs [11, 12]; however, inhibitory effects on tumor growth and metastasis have also been reported [13, 14].

An investigation of SN impact on the TME requires precise targeting of the somatic afferent fibers supplying the tumor. This represents a significant technical challenge for application to many types of solid tumor models, with the murine anatomy relevant to cutaneous sensory innervation being ideally suited for such studies. Specifically, surgical access to the peripheral neurons composed primarily of sensory fibers, as well as their dorsal root ganglia (DRG), provides a unique opportunity to study the impact of SNs on skin-associated malignancies. In this regard, cutaneous sensory innervation has been shown to contribute to tumorigenesis and cancer progression in the skin. For example, basal cell carcinoma arises preferentially within the mechanosensory touch dome epithelia [15]. We have previously shown that sensory DRG co-inoculated with orthotopic melanoma results in accelerated tumor growth *in vivo* [16]. However, selective cutaneous sensory denervation in the context of skin cancer progression has been heretofore understudied.

Melanoma is by far the most aggressive form of skin cancer, with a steadily increasing incidence worldwide [17]. The host immune system response to melanoma is essential to restricting cancer progression, with the magnitude and functional phenotypes of

tumor infiltrating lymphocytes (TILs) serving as predictors of patient clinical outcome and response to immunotherapy [18]. Hence, the development of therapies promoting a proinflammatory TME is of significant translational interest. We have previously reported that SNs and peripheral neuroglia, specifically Schwann cells (SCs), influence immune cell composition within the TME of melanomas [10, 16, 19–21]. However, a direct link between SN-modulated immune responses and melanoma progression has never been confirmed.

Utilizing surgical and chemical sensory denervation methods, we investigated the role of SNs in melanoma progression in mouse models. Both denervation methods significantly slowed the growth of subcutaneous B16F10 melanomas *in vivo*, without significantly affecting tumor-associated blood or lymphatic vascular densities. Depletion of $CD8^+$ lymphocytes prevented denervation-restricted tumor growth. We showed that sensory denervation led to the development of augmented melanoma-specific immune responses. When compared with controls, denervated tumors contained higher densities of mature high endothelial venules (HEV) associated with the formation of classical tertiary lymphoid structures (TLSs), which associate with a more favorable melanoma prognosis [22, 23]. Furthermore, tumors arising within denervated skin demonstrated improved recruitment and activation of both myeloid and lymphoid cells, reduced presence of regulatory immune cells, increased type-1 polarization of TILs, an increased T-cell clonality and expanded B-cell repertoire when compared with control tumors. Transcriptional profiling of human melanomas confirmed our findings in murine melanoma models. Specifically, the content of neuron-associated mRNA in human melanoma inversely correlated with anti-tumor immune response and TLS formation pathways and predicted superior overall survival. Our results implicate sensory innervation as an immunoregulatory mechanism within the melanoma TME that deserves attention as a target for the development of interventional therapeutic strategies to improve patient outcomes.

MATERIALS AND METHODS

Cell lines

B16F10 murine melanoma cells (ATCC, CRL-6475) were cultured in RPMI-1640 (Cytiva, SH30255.01), supplemented with 10% FBS (R&D Systems, S11550H), 0.1% 2-mercaptoethanol (Gibco, 21985–023), 1% Antibiotic Antimitotic Solution (Sigma, A5995), 1% HEPES (Gibco, 15630–080), 1% NEAA Mixture (Lonza, 13–114E), 1% L-Glutamine (Gibco, 25030–081). Cells were used at passages (P) 3–6 for tumor initiation.

Animals

All studies were conducted in accordance with the NIH guidelines for the Care and Use of Laboratory Animals and approved by the Institutional Animal Care and Use Committee of the University of Pittsburgh (Pittsburgh, PA). C57BL/6 mice (8-week-old) were purchased from the Jackson Laboratory and were housed in a pathogen-free facility under controlled temperature, humidity, and 12-hour light/dark cycle with a commercial rodent diet and water available ad libitum. The Plp-CreERT/tdTomato$^{f/f}$ mice were generated by crossing B6.Cg-Tg(Plp1-cre/ERT) (Jackson Lab, Stock No: 005975) with B6.Cg-Gt(ROSA)26Sor$^{tm14(CAG-tdTomato)}$) (Jackson Lab, Stock No: 007914). To induce

Cre recombination, tamoxifen (Sigma, T5648) in corn oil (20 mg/mL) was injected intraperitoneally (75 mg/kg) every 24 hours for five consecutive days.

Animal models

Surgical sensory cutaneous denervation was adapted from a previously described technique [24]. Briefly, C57BL/6 mice were anesthetized with isoflurane (Covetrus, 11695067772), using single animal vaporizer unit (E-Z Systems, 108SA) at a flow rate of 2 L/minute, and an approximately 1.5 cm skin incision was made along the midline back skin. Six dorsal cutaneous sensory nerves on the left side were tied off with 9–0 prolene sutures (Ethicon, 1754G) at their bifurcation from the main nerve trunk. Nerves were transected approximately 2 mm distally to the sutures, carefully dissected, and 5–7 mm of distal nerves were removed. Skin was sutured with 7–0 prolene sutures (Covidien, SP-1696G). Sham surgery included skin incision without nerve transection. Two months after surgery and prior to melanoma injection, complete local sensory denervation on left back and flank was confirmed with pin prick test. Chemical sensory denervation was performed as previously described.[25] Resiniferatoxin (Cayman Chemical) was injected intraperitoneally at escalating doses of 30 μg/kg, 70 μg/kg, and 100 μg/kg for three consecutive days. Denervation was confirmed by tail flick response to noxious heat stimulation after 21 days. Denervated and age-matched control mice were injected intradermally with B16F10 melanoma cells (10^5 cells in 100 mL sterile PBS) into the left dorsolateral skin. Tumor area (mm^2) was measured with a caliper every second day starting at day seven. To deplete $CD8^+$ T cells, a previously described method was utilized.[26] Briefly, mice were injected i.p. with 150 μg anti-mouse CD8a (clone 2.43; BioXcell) on days 0, 3, 6, 9 after B16F10 injection. CD8 depletion was confirmed by flow cytometry analysis of splenocyte single-cell suspensions utilizing non-overlapping anti-mouse CD8a (clone CT-CD8a, ThermoFisher). Rat IgG2b kappa antibody (clone LTF-2, BioXcell) was used as isotype control.

Flow cytometry

On days 16–17 after B16F10 cell injections, tumors were harvested and minced, incubated in DMEM (Corning, 10–013CV) containing collagenase D (1 mg/mL, Sigma, COLLD-RO) and DNase (1 mg/ mL, Sigma, DN25–1G) for 45 minutes at 37°C, and passed through 70 μm cell strainers (Falcon, 352350). Spleens and inguinal lymph nodes were passed through 70 μm cell strainer, washed in MACS buffer (Miltenyi Biotec, 130-091-221), and incubated for 5 minutes at 4°C in 2 mL of RBC lysis buffer (Biolegend, 420302). Single-cell suspensions were stained in MACS buffer with surface antibodies and Fixable Viability Dye eFluor 780 (FVD, Invitrogen, 1:1000) for 1 hour at 4°C. For intracellular staining, cells were first fixed and permeabilized with the FoxP3/Transcription Factor Staining kit (eBiosciene) for 30 minutes at room temperature, stained with surface antibodies and FVD, followed by incubation with intracellular and intranuclear antibodies for 60 minutes at room temperature. Flow cytometry was performed on BD LSRFortessa (BD Biosciences), and data analyzed using FlowJo software (BD Biosciences, flowjo.com). Antibodies used are listed in Supplementary Table S1. Gating strategy and parameters are provided in Supplemental Material.

IFNγ ELISAs

Spleens and inguinal lymph nodes of tumor-bearing mice 16 days after B16F10 cell injection were harvested, dissociated as indicated above, passed through a 70-μm cell strainer, washed once with PBS, and incubated for 5 minutes at 4°C in 2 mL of RBC lysis buffer. Cell mixtures were co-cultured with irradiated B16F10 cells (10^4 Rads, Gammacell 1000 Elite, Nordion) at a 20:1 ratio (leukocytes/melanoma cells), 37°C in RPMI containing IL15 (PeproTech, 10 ng/mL) for 5 days. Cells were washed in PBS, split, and co-incubated with B16F10 cells (10:1 ratio) in RPMI media for 24 hours. IFNγ in 10 μl supernatants (1:10 dilution) were determined using the Mouse IFNγ ELISA Set (BD Biosciences), based on standard curves obtained utilizing the kit IFNγ, according to the manufacturer's protocol. Measurements were performed with iD5 plate reader (Molecular Devices) and analyzed using SoftMax Pro 7.1 (Molecular Devices).

Immunofluorescence (IF)

Tumors were harvested at days 16–17 after B16F10 cell injections. Tissues were fixed with 2% paraformaldehyde (PFA) for 2 hours, incubated in 30% sucrose in PBS for 24 hours, frozen in 2-methylbutane (Sigma) in liquid nitrogen, embedded in Tissue Plus OCT (Thermo Fisher), and processed into 50 μm thick sections. Sections were permeabilized with 0.1% Triton X-100 (Sigma, T9284) in PBS for 10 minutes, blocked with 5% goat serum (Gibco, 16210–072) with 2% BSA in PBS for 45 minutes, and washed with 0.5% BSA in PBS. Immunostaining was performed for 16 hours at 4°C with primary antibodies (Supplementary Table S2), followed by secondary antibodies (Supplementary Table S2) for 1 hour at room temperature and then 4′,6-diamidino-2-phenylindole (DAPI, Sigma, 1 μg/mL). Sections mounted in gelvatol medium (Sigma) were imaged using Nikon A1+ confocal microscope. Image analyses were performed with NIS-Elements AR 4.40 software (Nikon).

Real-time (RT)-PCR

For RNA extraction, mouse B16F10 tumors stored in RNAlater (Invitrogen) were homogenized in TRIzol Reagent using a bead homogenizer Bullet Blender (Next Advance) at speed 8 for 5 minutes using Navy Rhino tubes (Next Advance, NAVYR1). RNA was isolated using TRIzol Reagent (Thermo Fisher) as per the manufacturer's protocol and quantified using DeNovix DS-11 spectrophotometer. For cDNA synthesis, 2 μg RNA was converted to cDNA using a QuantiTect Reverse Transcription Kit (Qiagen). Quantitative (q)RT-PCR was performed using TaqMan probes labelled with FAM-ZEN/IBFQ (Supplementary Table S3), an endogenous control (*Actin*) labelled with VIC-MGB-PL, and TaqMan Fast Advance Master Mix (Applied Biosystems). For select gene targets, qRT-PCR was performed using Fast SYBR Green Master Mix (Applied Biosystems) with appropriate primers (Supplementary Table S3), and *Gapdh* as endogenous control. Reactions were run and analyzed on StepOnePlus thermocycler (Applied Biosystems). Relative fold changes were calculated and normalized based on $2^{-\Delta\Delta Ct}$ method.

RNA-sequencing (RNA-seq)

RNA-seq was performed as previously described, with several modifications [10]. Briefly, TRIzol Reagent (ThermoFisher, 15596018) was used to extract total RNA from

homogenized tumors 16 days after B16F10 cell injections as described for qRT-PCR. Quality and concentration of RNA were determined with Qubit (ThermoFisher) and Agilent Bioanalyzer, and samples with RNA integrity numbers (RINs) 7.5 – 8.7 were used. Sequencing libraries were constructed by using Illumina TruSeq Stranded mRNA Prep with a read length of 2×75bp. Approximately 1.5×10^8 total reads, paired end, were obtained per tumor (Illumina NextSeq 500/550 v2.5 Mid Output, 150 cycles). The reverse stranded paired-end RNA-seq reads were checked for presence of adapters and high-quality bases using FastQC (v 0.11.9). The raw fastq files were lane separated, which required concatenation to generate complete, paired end fastq files. The universal adapters in the high-quality reads were already trimmed, and, therefore, did not require the use of an adapter trimming tool. The reads were mapped against the Ensembl mouse reference genome (GRCm38 mm10) using the HISAT2 (v 2.1.0) mapping tool. The output file from HISAT2 was converted from SAM format to BAM format using SAMtools (v 1.10). Counts for expressed genes were generated using HT-Seq (v 0.11.2) and were output in text format. These count text files were imported into the Bioconductor R-package, edgeR (v 3.32.1), which was utilized to identify the differentially expressed genes (DEGs) based on the criteria of the genes having an expression count of absolute value log base 2 greater than 1 between two experimental conditions and a false discovery rate (FDR) < 0.1. After DEGs were identified, the list of genes with their differential expression values were uploaded to Ingenuity Pathway Analysis (IPA, Qiagen). Gene Ontology (geneontology.org) and Enrichr (maayanlab.cloud/Enrichr) were also utilized for pathway analyses. Bar graphs were generated using R-package ggplot2 (v 3.3.5). Heatmaps were generated using R-package gplots (v 3.1.1).

Human melanoma TCGA analyses

The Cancer Genome Atlas (TCGA) program was used to obtain RSEM normalized RNA-seq data for 473 patients with skin cutaneous melanoma (SKCM)[27]. Eighty-two patients were selected whose RNA-seq data represented the primary melanoma tumor, not a metastatic lesion, and was procured prior to any interventional treatment. Patients were divided into two groups based on the sum of transcript per million (TPM) values of gene sets discussed in Results. Median value of summed TPM score was used to partition patients into high- and low-neuronal content groups (Supplementary Table S4), and DEGs between these two groups were determined using DESeq2 [28]. Genes upregulated in low-neuronal content group (vs. high-neuronal content group) with $p<0.05$ and fold change greater than 1.5 were utilized in pathway analyses with IPA and Enrichr. Bar graphs were generated using R-package ggplot2 (v 3.3.5). Kaplan-Meier analyses and log-rank test were performed using R-package survival (v 3.2–13).

Human melanomas

Primary cutaneous melanoma tissues were collected after obtaining signed informed consent from three subjects. Samples were processed and analyzed by IF as described above for mouse melanomas, utilizing primary and secondary antibodies listed in Supplementary Table S2. The study was performed after the approval by the institutional review board of the University of Pittsburgh, in accordance with an assurance filed with and approved by the

U.S. Department of Health and Human Services and was conducted in accordance with U.S. Common Rule ethical guidelines.

Immuno-sequencing of T-cell and B-cell receptor repertoires

Genomic DNA from whole tumors was extracted on day 16 after B16F10 cell injections, purified using DNAeasy Blood and Tissue kit (Qiagen), and shipped frozen to Adaptive Biotechnologies (Seattle, WA). Amplification was carried out utilizing TCRβ and BCR heavy chain (IgH) V/J gene-targeting multiplexed primers, and sequencing of CDR3 regions was performed as previously described.[29, 30] Potential amplification bias was measured and corrected using synthetic templates mimicking natural V(D)J rearrangements [29]. Productive rearrangements excluded out of frame sequences and sequences with stop codons within the CDR3 region. Data were analyzed using the ImmunoSEQ™ analysis platform (Adaptive Biotechnologies).

Statistical Analyses

Results are expressed as mean ± SD. Two-group analyses were performed using unpaired student's t test. Three or more groups with one independent variable were analyzed using one-way ANOVA with Tukey's multiple comparisons test. Three or more groups with two independent variables were analyzed using two-way ANOVA with Tukey's multiple comparisons test. Analyses were performed using GraphPad Prism software. All tests were two-tailed, and a p-value < 0.05 was considered to indicate statistical significance.

Data Availability Statement

RNA sequencing raw data are available in GEO database under accession number GSE193065. Immunosequencing raw data are available at https://doi.org/10.21417/OK2022MELANOMA. All data published in this report are available on reasonable request.

RESULTS

Sensory nerve ablation in the skin slows melanoma growth

Surgical denervation of dorsal thoracic sensory cutaneous fibers (Fig. 1A) was achieved with a modification of a previously reported method [24]. Briefly, proximal trunks of the transected and stripped nerves were intraoperatively tied with sutures (Supplementary Fig. S1A–B), thereby preventing axon sprouting and reinnervation, and resulting in complete, reproducible, and durable sensory cutaneous denervation associated with the loss of nociception of the back skin (see Methods). Immunofluorescence (IF) analyses of axonal and glial markers demonstrated a significant reduction in numbers of cutaneous neurons after surgical sensory denervation (SSD), including thick dermal and thin subepidermal nerve bundles, as well as free epidermal nerve endings (Supplementary Fig. S1C). To verify denervation, we also utilized transgenic mice, Plp-CreERT/tdTomato$^{f/f}$ (B6 background), which undergo tamoxifen-mediated expression of red fluorescent protein in the Schwann cells of the peripheral neurons (Supplementary Fig. S1D–E).[31–33] Using this model, we confirmed loss of the cutaneous neurons after SSD (Fig. 1B). Next, we examined whether SSD impacted vascular and lymphatic composition of the skin. Neither the density of CD31$^+$

vascular nor Lyve-1$^+$ lymphatic endothelial networks in denervated skin were affected by SSD (Supplementary Fig. S1F–H).

We next examined the rate of B16F10 melanoma growth in the surgically denervated skin of syngeneic C57BL/6 mice. Compared to control mice, SSD resulted in significantly slowed tumor growth (Fig. 1C–D). In contrast, sham surgery (skin incision and undermining without nerve transection) did not affect tumor growth. To confirm these results using a non-surgical complementary method, we administered resiniferatoxin (RTX), a potent agonist of transient receptor potential cation channel, subfamily V, member 1 (TRPV1), which selectively ablates TRPV1$^+$ neurons [25]. Intraperitoneal injection of RTX led to the loss of nociceptive cutaneous TRPV1$^+$ nerve fibers and their corresponding SC (Fig. 1E), which was confirmed in mice one month later based on their lack of response to noxious heat stimulation (see Methods). Similar to SSD, chemical denervation of the afferent cutaneous neurons resulted in a significantly slower growth rate for B16F10 melanomas *in vivo* (Fig. 1F). As we had observed in surgically denervated non-tumor bearing skin, densities of intratumoral CD31$^+$ vascular and Lyve-1$^+$ lymphatic vessels were not affected by the loss of SNs (Fig. 1G–H). The expression of tissue hypoxia marker, Hif1a, also remained unchanged in tumors after SSD (Fig. 1I). We next examined whether intervention-induced anti-melanoma immune responses contributed to slowed tumor growth after SSD. Antibody-mediated depletion of CD8a$^+$ T lymphocytes [26] at the time of tumor development abrogated the effect of SSD on melanoma growth (Fig. 1J), suggesting that sensory innervation of the skin supports melanoma progression by regulating local immune responses to tumor cells.

Sensory skin denervation promotes immunocompetent TME

Further investigation revealed that compared to controls, tumors arising within surgically denervated skin contained more CD45$^+$ leukocytes (Fig. 2A, Supplementary Fig. S2). The percentages of infiltrating CD4$^+$ and CD8$^+$ T cells, CD19$^+$ B cells, and CD11b$^+$ cells were all elevated in the denervated TME, whereas frequency of F4/80$^+$ macrophages remained constant (Fig. 2B). Significantly fewer regulatory T cells (T_{reg}) were found in the SSD tumors vs. control tumors (Fig. 2C), and intratumoral percentages of F4/80$^+$CD206$^+$ M2 tumor-associated macrophages (TAMs) and Ly6G$^+$ granulocytic myeloid-derived suppressor cells (MDSCs), but not Ly6G$^-$Ly6C^{hi} monocytic MDSCs, were also diminished after SSD (Fig. 2D). Significantly fewer CD8$^+$PD-1$^+$ and CD4$^+$PD-1$^+$ T cells were identified in denervated tumors, suggesting that these effector cells were less exhausted and presumably functionally competent (Fig. 2E)[34]. Finally, CD4$^+$ T cells expressing CD73, an ecto-5′-nucleotidase that catalyzes the conversion of extracellular AMP to adenosine, a potent immunosuppressive factor in TME [35], were found less frequently in denervated tumors (Fig. 2F). Flow cytometric analyses of TILs from RTX-denervated mice confirmed the findings obtained in our surgically denervated animal models (Supplementary Fig. S3).

In contrast to the TME, the spleens of mice after SSD or RTX-mediated sensory ablation did not exhibit altered immune profiles compared to spleens isolated from control animals, with the exception of a decrease in splenic CD8$^+$PD-1$^+$ T-cell content after SSD (Supplementary Fig. S4–S6). The composition of immune cells in the TME after CD8a-depletion was not

reflective of the status of cutaneous sensory innervation (Supplementary Fig. S7). CD8a-depletion led to diminished populations of T cells ($CD8^+$, $CD4^+$, T_{reg}), but not $CD11b^+$ cells, in control and denervated tumors; the only significant difference between the two groups was fewer intratumoral $CD11b^+F4/80^+$ cells after SSD (Supplementary Fig. S7). Spleens of both the innervated and denervated groups displayed a 15-fold decrease in $CD8^+$ T cells after CD8a-depletion relative to non-depleted controls (Supplementary Fig. S8). The only two significant differences in the composition of splenic immune cells between the CD8a-depleted innervated and CD8a-depleted denervated groups were increased frequencies of $CD4^+PD\text{-}1^+$ and $CD8^+PD\text{-}1^+$ populations in the latter cohort (Supplementary Fig. S8). The changes in the TME immune composition fomented by skin denervation were only observed in tumor-bearing mice. Specifically, when we compared non-tumor bearing control mice to non-tumor bearing denervated mice, we did not observe any differences in either the composition or the phenotype of lymphoid and myeloid immune cells in their skin, inguinal lymph nodes, or spleens (Supplementary Fig. S9). These results suggest that the absence of sensory innervation in the skin leads to a more immunocompetent and protective cutaneous TME.

The density of $CD8^+$ TILs in melanoma has long been considered a positive prognostic marker of patient overall survival and response to (immuno)therapy [18]. IF confirmed our flow cytometry results, with $CD8^+$ TIL densities in skin tumors devoid of SNs being significantly higher than those found in innervated tumors (Fig. 3A–B). To elucidate their functional status, we determined the percentages of interferon (IFN)γ^{hi} and granzyme (Gzm)-B^{hi} $CD8^+$ TILs by flow cytometry. In surgically denervated melanoma-bearing mice, more $CD8^+$ TILs were IFNγ^{hi}, whereas the percentage of $GzmB^{hi}$ cells among $CD8^+$ TILs remained unchanged compared to controls (Fig. 3C). IFNγ^{hi} and $GzmB^{hi}$ $CD8^+$ TILs in the TME of RTX-treated mice were significantly increased relative to controls (Fig. 3D). TME expression of *Ifng* from surgically and chemically denervated skin was also increased relative to tumors isolated from skin with intact nerves (Fig. 3E). To further determine whether melanomas elicited stronger effector T-cell responses in denervated mice, single-cell suspensions of lymph nodes and spleens from control and denervated tumor-bearing mice were isolated and restimulated with B16F10 melanoma cells *in vitro*. Lymphocytes obtained from the inguinal lymph nodes and spleens of surgically denervated tumor-bearing mice produced significantly more IFNγ in response to melanoma restimulation *in vitro* vs. those isolated from control mice (Fig. 3F). Sensory denervation with RTX yielded similar results (Fig. 3G). These findings suggest that anti-tumor T-cell responses in denervated mice are superior to those in mice with intact sensory cutaneous innervation.

To better understand the impact of denervation on the immune responses to melanoma, we performed RNA-seq analyses of B16F10 tumors isolated from the skin of control vs. SN-depleted mice. Of the 409 differentially expressed genes (DEGs) with a 0.1 false discovery rate (FDR) cutoff, 364 were upregulated and 44 were downregulated (Supplementary Table S5). Several of the downregulated genes, including *P2rx3*, *Kcnh2*, *S100β*, *Slc6a9*, *Abat*, *Kcnn1*, *Avil* were highly expressed by neurons or by select non-PNS cells in response to neuronal signals. Gene Ontology (GO) analysis of the 44 downregulated genes revealed enrichment of a single pathway: Positive Regulation of Nervous System Process (GO:0031646, p=2.09e-6, FDR=3.3e-2, 48-fold enrichment), suggesting an expected

reduction in neuronal signaling in the TME after SSD. Corroborating our flow cytometry findings, expression of *Ptprc* (CD45), *Cd4*, *Itgam* (CD11b), and *Itgax* (CD11c) were significantly increased in denervated tumors relative to controls (Supplementary Table S5). Utilizing Ingenuity Pathway Analysis (IPA) and considering all 409 DEGs, we found that the majority of the most significantly enriched pathways (lowest p-values) broadly reflected the activation of anti-cancer immune responses (Fig. 4A, Supplementary Table S6). Pathway analysis with Enrichr confirmed denervation-dependent activation of innate and adaptive immune response elements, which could be subdivided into the following categories: activation of the immune response, leukocyte adhesion and diapedesis, Th1 and Th2 responses, B-cell activation, antigen processing and cross-presentation, and interferon signaling (Supplementary Fig. S10, Supplementary Table S7). We also examined enriched physiological pathways using IPA, which could be parsed into the following groups: recruitment, homing, adhesion, transmigration, chemotaxis and activation of leukocytes (T and B lymphocytes, antigen-presenting cells), and formation/quantity of lymphoid tissue (Fig. 4B, Supplementary Table S8). Taken together, these data corroborate superior activation of multiple branches of the protective host immune response within the cutaneous TME lacking sensory innervation.

Skin sensory nerve ablation stimulates the formation of TLS-like structures in TME

The appearance of the “lymphoid organ formation” pathway in our RNA-seq results led us to further investigate the relationship between SSD and TLSs in the melanoma TME. TLSs are ectopic lymph node-like structures containing variably organized B- and T-cell aggregates surrounding lymphatic and high endothelial blood vessels [36], and have been identified in several types of cancer, including melanoma [37, 38]. _ENREF_32 The presence and the extent of TLS formation in the melanoma TME are predictive of favorable patient response to immunotherapy and extended overall survival [22, 23]. TLSs in tumors may amplify cytokine-mediated signaling, improve antigen presentation and tumor-specific antibody production [39]. In pancreatic carcinomas, small nerve fibers have been reported to associate with lymphoid aggregates, but the relationship between TLSs and innervation in tumors remains poorly understood [40]. Based on the results of our transcriptional profiling of the TME, we next examined the association between sensory nerves and TLS formation in our cutaneous melanoma model. From the 409 DEGs, we identified 54 genes previously associated with TLS formation [22, 39, 41–43]. Expression of all the gene products in this *ad hoc* panel were upregulated in denervated tumors (Fig. 4C). We also assessed expression of consensus pro-TLS factors, including chemokines associated with inflammatory infiltrates and TLS formation [38, 41, 44]. We observed that expression of *Ccl3*, *Ccl5*, *Ccl19*, *Ccl21*, *Cxcl9*, *Cxcl13*, *Tnfa* were all upregulated in melanomas lacking sensory innervation (Fig. 4D). Compared with control tumors, denervated tumors also expressed elevated lymphotoxin β receptor (LTβR) agonists *Lta*, *Ltb*, and *Tnfsf14/LIGHT*, which are implicated in secondary lymphoid organ (SLO) and TLS development (Fig. 4E)[39, 41, 42]. IPA pathway analyses similarly revealed an enrichment trend (p=0.07) for lymphotoxin β receptor signaling in denervated tumors (Supplementary Table S6). Cumulatively, these results suggest that SSD promotes TLS formation in the cutaneous melanoma TME.

To expand on these findings, we morphometrically analyzed melanoma tumors for the physical presence of TLSs. As in the case of SLO, tumor-associated TLSs contain high endothelial venules (HEVs), specialized postcapillary venules expressing high sulfated sialomucins which mediate homing and transmigration of lymphocytes from the blood [36, 37, 39]. Sulfated sialomucins, ligands for L-Selectin/CD62L, are concentrated on high endothelial cells (HECs) and serve as classical biomarkers for HEVs. Our genomic analyses revealed a trend for upregulated expression of several gene products associated with sialomucins in denervated versus innervated tumors, including *Cd34* (FC=1.59, p=0.0199), *Podxl* (FC=1.5, p=0.0538), and *Emcn* (FC=1.58, p=0.0445). qRT-PCR analyses confirmed upregulation of *Cd34*, *Podxl*, and *GlyCAM1* in tumors after SSD (Fig. 4F). Expression of other HEV leukocyte-homing receptors [45], *Icam1* and *Selp*, were also increased after denervation (Fig. 4C, 4F). Expression of chemokines present on the luminal surface of HEVs, which mediate lymphocyte trafficking,_ENREF_46 including *Ccl19* and *Ccl21* (and their receptor *Ccr7*), *Cxcl9*, *Cxcl12*, *Cxcl13*, were also upregulated in denervated tumors (Fig. 4C–D). We also found that tumors from denervated skin expressed elevated HEC/HEV adhesion molecules, including *Vcan* (FC 2.5, p=0.0058), *Mcam* (FC 1.47, p=0.011), *Fxyd5* (FC 1.63, p=0.012), *Icam1* (FC 3.71, p=4.17e-5), *Vcam1* (FC 4.44, p=1.2e-7) (Fig. 4C, F; Supplementary Table S5)[39, 45, 46]. Ligands of these leukocyte homing domains, such as *Itgb2*, *Itgb7*, *Itgal*, and *Selplg*, also had higher expression in denervated vs. innervated tumors (Fig. 4C, Supplementary Table S5).

To further quantify and characterize HEVs in B16F10 melanomas, we used IF and MECA-79 antibody, which binds sulfated peripheral node addressin (PNAd) of HECs [47]. The fluorescence intensity of HEVs stained with anti-MECA-79 was significantly elevated in denervated tumors versus controls (Fig. 5A–B). HECs in denervated tumors exhibited a more pronounced cuboidal morphology and contained more CD34 and ICAM1 vs. HECs in control tumors (Fig. 5A–B). Using IF, we also examined the extent of lymphocyte clusters surrounding $PNAd^+$ HEVs as an indicator of TLS formation. In SN-ablated tumors, $PNAd^+$ HEVs had denser adjacent aggregates of $CD3^+$, $CD4^+$, and $B220^+$ lymphocytes (Fig. 5C–F). CD8a depletion prior to melanoma initiation significantly diminished peri-HEV $CD3^+$ and $B220^+$ cells in denervated tumors (Supplementary Fig. S11) To better determine whether $PNAd^+$ HEVs and TLS in melanomas form near nerves, we examined B16F10 tumors isolated from the skin of Plp-CreERT/tdTomato$^{f/f}$ mice. We observed that nerves were located in close proximity to $PNAd^+$ HEVs in innervated but not SSD tumors, as expected (Fig. 5G). The absence of nerves near $PNAd^+$ HEVs, therefore, correlated with significantly larger clusters of $CD3^+$ lymphocytes around the tumor-associated blood vessels (Fig. 5G). When taken together, these findings suggest that SN ablation in the cutaneous TME promotes maturation of HEVs, infiltration by immune cells, and their organization into TLSs.

Sensory nerve ablation in skin expands T-cell and B-cell repertoires in TME

As in the case of SLO, tumor TLSs are posited to serve as local sites for T- and B-lymphocyte recruitment, antigen presentation, and the generation of tumor-specific effector T-cell and antibody responses. In melanoma and other cancers, naïve $CD62L^+$ T cells are recruited into TLSs within the TME, where they are (cross)primed, expanded, and

differentiated into effector cells that mediate anti-tumor immunity [48, 49]. Increased densities and the maturation of TLSs in tumors has been linked to expansions in the (anti-tumor) T- and B-cell repertoires [49–52]._ENREF_48 We, therefore, determined the effect of sensory innervation on the intratumoral T-cell (TIL-T) and B-cell (TIL-B) repertoires. We performed TCR-seq of V(D)J complementarity-determining region 3 (CDR3) of TCRβ rearrangements on control vs. denervated melanomas [29, 30]. We found that the number of unique TCRβ clonotypes was not significantly different between the two groups, indicating that the TIL-T population richness is not impacted by the absence of intratumoral sensory nerves (Fig. 6A). Simpson clonality, however, was significantly increased in denervated tumors, indicating a reduced evenness (i.e., increased oligoclonality) of TCRβ rearrangements in the TIL-T population (Fig. 6B). The frequency of the most represented TCRβ clonotypes among all productive rearrangements was elevated in SSD tumors relative to controls (Fig. 6C), as was the sum of the frequencies of the top 5 most abundant TCRβ clonotypes (Fig. 6D, Supplementary Fig. S12). Differential analysis of the clonotypes with abundance > 5 shared between control and denervated tumors, but were represented at a significantly higher frequency in either group, revealed a trend suggestive of local, intratumoral expansion (increase in frequency) of these shared TCRβ clonotypes in the SSD group (Fig. 6E–F), and the number of unique TCRβ clonotypes with abundance > 50 was significantly increased in denervated tumors relative to controls (Fig. 6G–H). Analysis of the overlapping datasets suggested a trend for an increase in the number of shared CDR3 sequences (amino acids) among the denervated tumors, as well as between denervated and control tumors, relative to the shared sequences among the control tumors (Fig. 6I–J). Overall, these results suggest that sensory denervation leads to clonal expansion of shared and unique TIL-T clonotypes in association with enhanced TLS formation in the TME.

We also analyzed TIL-B repertoire by immune-sequencing the BCR H chain (IgH) CDR3 region on whole tumor explants [29]. The number of unique BCR IgH clonotypes, a reflection of clonal diversity (richness), was significantly increased in SSD tumors relative to controls (Fig. 6K). Simpson clonality, a measure of the population clonal polarization, showed a decreasing trend in tumors with ablated nerves (Fig. 6L). The fraction of productive BCR rearrangements, in frame rearrangements without a stop codon that can generate a functional protein receptor, was increased in TIL-B populations isolated from denervated tumors (Fig. 6M), and the sum frequency of the top 5 intratumoral BCR IgH clonotypes was not affected by SSD (Fig. 6N). When taken together, these results confirmed our RNA-seq, IF, qRT-PCR, and flow cytometry analyses in supporting that sensory nerve ablation leads to increased recruitment and expansion of B-cells into/within the melanoma TME. An increase in intratumoral BCR clonal diversity at the expense of clonal polarization in denervated mice suggests that TIL-B clones may have been preferentially recruited from SLO rather than generated in TLSs. Indeed, whereas B-cells were significantly more numerous around $PNAd^+$ HEVs of SSD vs. innervated tumors on days 14–21 post melanoma implantation (Fig. 5), we did not observe formal germinal center formation in the TME at these time points (with germinal centers postulated to serve as local sites for B-cell clonal expansion and somatic recombination in TLS *in situ*)[23].

A neuron-associated gene signature negatively correlates with immune response in human melanoma and predicts overall survival

We next determined whether the negative correlation between skin sensory innervation and the enhanced development of anti-tumor immune responses observed in our mouse models was reflective of human disease. To that end, we performed analyses of skin-cutaneous melanoma (SKCM) RNA-seq data publicly available from The Cancer Genome Atlas (TCGA). From gene expression profiling data (n=473 melanoma samples), we selected 82 primary cutaneous lesions that were procured prior to any interventional treatment. Patients were divided into two groups based on the summed tumor-associated expression score (transcripts per million, TPM) composed of seven genetic markers associated with sensory neurons: *Scn10a*, *Calca*, *Tac1*, *Gal*, *Nefh, Kcnn1*, *Kcnh2* (Supplementary Table S4)[53]. These genes were chosen based on their expression specificity in sensory neurons in both mice and humans [54, 55]. Two of these genes, *Kcnn1* and *Kcnh2*, were downregulated in our surgical denervation mouse model (Supplementary Table S5). Because melanocytes and the PNS share a common neural crest cell origin, we excluded neuronal and glial genes known to be expressed by melanoma cells [56]. Human primary melanomas with summed TPM expression scores of these seven genes larger than the overall group median were considered as having higher neuron-associated mRNA content (NAmRNA), and *vice versa* (Fig. 7A). High and low NAmRNA content groups did not differ based on a range of other parameters, including age, gender, ethnicity, pathological stage, or site of disease (Supplementary Table S9).

Analysis of DEGs between the high and low NAmRNA groups was then carried out. Multiple pro-inflammatory cytokines, chemokines, and other immune mediators were significantly upregulated in the low vs. high NAmRNA group, including *Ccl2*, *Ccl7*, *Ccl8*, *Ccl13*, *Cxcl5*, *Cxcl13*, *Tnfsf13*, *Il6*, *Il15*, and others (Supplementary Table S10). Pathway analyses with IPA (Supplementary Table S11) and Enrichr (Supplementary Table S12) revealed an enrichment of identical immune response pathways in the low NAmRNA group to those we observed in our SSD mouse model. Specifically, pathways involving the activation of antigen processing and presentation, TCR and BCR signaling, and interferon gamma signaling were upregulated in the human melanomas with low levels of neuron-associated transcripts (Fig. 7B, Supplementary Fig. S13A). Physiological IPA pathways enriched in the low NAmRNA group - recruitment, homing, transmigration and chemotaxis of lymphoid/myeloid cells, lymphopoiesis and formation of lymphoid tissue - were identical to the mouse denervation model (Fig. 7C, Supplementary Table S13). We performed IF to further evaluate the role of the innervation on TLS formation in human primary cutaneous melanoma. We detected $PNAd^+$ HEVs, which were either in close proximity to the $PGP9.5^+$ neurons or not associated with neurons and noted a significantly reduced density of $CD3^+$ lymphocytes around $PNAd^+$ HEVs, which were located next to nerves vs. HEVs with no near-neighbor neurons (Fig. 7D–E). Finally, because TLS formation has been shown to improve melanoma survival, we compared the available survival data in our high and low NAmRNA cohorts. Overall survival was significantly greater among patients with low NAmRNA melanomas (Fig. 7F). Because the unequivocal detection of local translation in primary afferents within tissues requires spatial transcriptomics [57], we grouped the same patient cohort based on tumor expression of 15 genes associated

with SCs (*Mag, Gdnf, Gap43, Ncam1, Gldn, Plp1, Ntn1, Prx, Ntf3, Ntf4, Ntrk3, Cntn2, Cntn4, GabbR1, Areg*), avoiding genes highly expressed by melanoma cells [58]. Analysis of DEGs in low vs. high SC mRNA content groups was carried out (Supplementary Table S14), which revealed an upregulation of pro-inflammatory and HEV maturation pathways, including leukocyte diapedesis and lymphotoxin β receptor signaling, in the low SC mRNA group (Supplementary Table S15). As in the case of NAmRNA analysis, overall survival was significantly greater among patients with low SC mRNA content melanomas (Supplementary Fig. S13B). Taken together, these data suggest that in mouse (and human) melanomas, the presence of sensory neurons (and neuron-associated mRNA content) in the TME may restrict local inflammation and TLS formation, thereby limiting protective anti-tumor immune responses in support of disease progression and reduced overall survival.

DISCUSSION

The main novel finding in our study reflects the regulatory role mediated by melanoma-associated sensory neurons on the development and function of immune responses within the TME. We observed that both complete surgical sensory denervation and chemical ablation of $TRPV1^+$ sensory neurons of cutaneous melanomas resulted in the activation of anti-tumor immune programming in the TME, as evidenced by a reduction in intratumoral T_{reg}, M2 TAM, and MDSC immunosuppressive populations, and a coordinate increase in effector immune cell presence. We did not observe any denervation-associated changes in the densities of vascular and lymphatic endothelial cells or expression of hypoxia markers in the denervated TME, suggesting that modulation of the immune system is a primary mechanism by which sensory neurons support melanoma growth in skin. In this regard, we observed that antibody-mediated depletion of $CD8^+$ T cells mitigated the effect of sensory nerve ablation on melanoma progression, supporting the key role of anti-tumor $CD8^+$ T cells in disease outcome. In the absence of sensory neurons, HEVs in the TME were more mature, and leukocyte recruitment into the TME was enhanced, with these immune cells orchestrated into non-classical TLSs lacking apparent germinal centers but containing dense clusters of T cells and B cells. The augmented influx of the myeloid and lymphoid cells into denervated melanomas also resulted in an expanded intratumoral BCR IgH repertoire and the increased (cross)priming of T cells, in association with an expanded T-cell repertoire and improved TIL effector functionality. These results suggest that tumor-associated sensory neurons ($TRPV1^+$ fibers, specifically) actively restrict the evolution of protective anti-tumor immune responses in the cutaneous TME *in vivo*.

TLS formation has been increasingly recognized as an important biologic process associated with a more favorable cancer patient prognosis and an indicator of superior patient response to immunotherapy [22, 23]. The evidence for a neuro-immune circuit regulating SLO and TLSs is only now emerging in the setting of select inflammatory conditions [53, 59, 60]. Very recently, nerve fibers were reported to co-localize with TLSs in pancreatic cancer [40], which has a dismal clinical prognosis and associates with severe immune dysfunction [61]. We present here, for the first time, experimental evidence supporting neuroimmune regulation impacting HEV maturation and TLS formation within the TME. TLSs serve as gateways for $CD62L^+$ naïve/central memory lymphocyte infiltration from blood into tumors, a function which is largely mediated by mature $PNAd^+$ HEVs [39].

Various inflammatory immune cells have been implicated in the neogenesis and maturation of HEVs in the TME, including both lymphoid ($CD8^+$ T cells, B cells, NK cells)[48, 62] and myeloid ($CD11c^+$ dendritic cells, $CD68^+$ macrophages)[62, 63] cells types. We observed that denervation was accompanied by a decrease in intratumoral populations of two major types of regulatory immune cells, T_{reg} and $Gr1^+$ neutrophils, which have previously been shown to inhibit TLS formation [64, 65]. We did not observe $CD11c^+$ clusters in TME-associated TLS-like structures in our models, which rather resembled canonical immature TLSs composed of $CD4^+$ T-cell and B-cell aggregates, but without formation of mature (B cell-rich) germinal centers. Although antibody-mediated $CD8a^+$ T-cell depletion abrogated the anti-tumor benefit provided by skin denervation, it remains mechanistically unclear exactly how sensory nerves impede TLS formation in tumors. We would hypothesize that afferent neurons may either directly hinder HEC maturation, block the recruitment or the activity of lymphoid tissue-inducing cells, or promote the infiltration of regulatory cells which are contraindicated for TLS formation (Fig. 7G). Clearly, further translational/clinical investigation of the dynamic interactions within the neuro-immune axis of the TME is warranted.

The functions of peripheral sensory neurons are tightly coupled to SC activity [66]. Because neurons are comprised of nerve fibers and SC, denervation methods aimed at removing one of these components inadvertently affects the other. Thus, complete surgical, chemical, or genetic ablation of the nerve/SC unit leads to challenges in determining relative contribution of either element to the observed phenotype [1]. We have previously shown that DRG neurons and SC may accelerate melanoma progression via neuro-regenerative and immunomodulatory mechanisms [10, 16]. Here, we utilized complimentary surgical and chemical denervation methods which removed the majority of sensory nerve fibers and SC from the skin prior to melanoma initiation. Therefore, it is impossible to conclude with certainty which of these components of the sensory neuron is responsible for hindering anti-tumor immunity in the TME. Additional cell-specific inducible non-ablative genetic models will be required to conclusively determine how afferent nociceptive fibers ($TRPV1^+$ and $TRPV1^-$ fibers) and/or their associated SC regulate local immune responses in the TME.

Our analyses of melanoma patient cohort should be interpreted with caution. Tumoral presence of transcripts commonly associated with DRG, which are located some distance from cutaneous tumors, does not directly indicate innervation, as these mRNAs may be from non-neuronal cells. Although local translation in primary afferent axons has been reported for a number of DRG-associated factors (including Gap43, Calca, Scn10A) [57], spatial transcriptomics and multiplexed quantitative tissue microscopy of patient melanomas and outcome measures must be performed to unequivocally determine the impact of tumor innervation on immune responses, TLS formation, and overall survival. Our data indicate that grouping patients based on the content of SC-associated transcripts in tumors also suggests an inverse relationship between tumor innervation and inflammation/overall survival. Other interpretations are possible, such as the relationship of neural-like differentiation of melanoma cells (neurotropic, desmoplastic) to an immunosuppressive TME and poor survival. However, clinical data does not currently support such an interpretation [67]. Further studies utilizing human melanomas are required to better

understand the impact of tumor afferent innervation on protective immune responses and disease progression.

Selective targeting of sensory neurons for cancer therapy has thus far not been realized. Ablation and deactivation of sensory innervation using varying methods in different mouse tumor models, including pancreatic, gastric, breast and skin cancers, has yielded conflicting results [11–16]. Such discrepancies may arise from organ-specific differences in tumor innervation or anti-tumor immunity, or other TME factors, as well as distinct SN-targeting techniques employed in these studies. Further reflecting this disparity, modulations of nociceptor signaling axes for cancer therapy have proven inconclusive. For example, substance P (SP), a tachykinin neuropeptide released by sensory neurons, was reported to promote cancer progression over a decade ago [68]. However, aprepitant, an antagonist of the neurokinin-1 receptor (NK1R which binds SP) used to treat chemotherapy-related nausea and vomiting, has thus far failed to demonstrate anti-tumor efficacy [69]. Targeting TRPV1, a capsaicin receptor expressed on nociceptor neurons, has been successful in the treatment of neuropathic pain, but its utility in cancer therapy remains equivocal [70]. The use of botulinum neurotoxins, which prevent neurotransmitter and neuropeptide release from the termini of afferent and efferent neurons, has similarly been limited to treating cancer-related pain, rather than being applied as a cancer therapeutic agent [71]. Further studies will be required to discern the impact of PNS-targeting drugs on immune status within the TME and how they may be combined with existing immunotherapies for possible synergistic treatment benefit in the cancer setting. In this regard, we detected upregulated expression of several anti-inflammatory factors in the denervated melanoma TME, including Arg1, Ptgs2/Cox2, and PD-L1, suggesting near-term assessment of combination protocols implementing local denervating agents along with agents that antagonize these compensatory (immuno)regulatory pathways, such as checkpoint inhibitors [72]. We further anticipate that prospective studies of SN-specific regulatory mechanisms in the cancer setting will likely identify additional therapeutic candidates for use in monotherapies or combination immunotherapies.

Supplementary Material

Refer to Web version on PubMed Central for supplementary material.

Acknowledgements

This project was supported by the Research Scholar Grant, RSG-19-088-01-CSM, from the American Cancer Society (YLB), and by the Hillman Fellows for Innovative Cancer Research Program funded by the Henry L. Hillman Foundation (YLB). This project utilized the University of Pittsburgh Imaging Core that is supported in part by award P01HL114453, and the Hillman Cancer Genomics Facility and Bioinformatics Services, supported in part by award P30CA047904. The results published here are in part based upon data generated by the TCGA Research Network: https://www.cancer.gov/tcga. The authors wish to thank Maureen A. Lyons for assisting with RNA sequencing, and Drs. Brian M. Davis and Daniel H. Kaplan for their careful reviews and helpful comments provided during the preparation of this manuscript.

Funding

This project was supported by the Research Scholar Grant, RSG-19-088-01-CSM, from the American Cancer Society (YLB), and by the Hillman Fellows for Innovative Cancer Research Program funded by the Henry L. Hillman Foundation (YLB). This project utilized the University of Pittsburgh Imaging Core that is supported in part by award P01HL114453, and the Hillman Cancer Genomics Facility and Bioinformatics Services, supported in part

by award P30CA047904. The results published here are in part based upon data generated by the TCGA Research Network: https://www.cancer.gov/tcga.

REFERENCES

1. Zahalka AH, Frenette PS. Nerves in cancer. Nat Rev Cancer. 2020;20: 143–157. [PubMed: 31974491]
2. Zahalka AH, Arnal-Estape A, Maryanovich M, et al. Adrenergic nerves activate an angio-metabolic switch in prostate cancer. Science. 2017;358: 321–326. [PubMed: 29051371]
3. Magnon C, Hall SJ, Lin J, et al. Autonomic nerve development contributes to prostate cancer progression. Science. 2013;341: 1236361. [PubMed: 23846904]
4. Albo D, Akay CL, Marshall CL, et al. Neurogenesis in colorectal cancer is a marker of aggressive tumor behavior and poor outcomes. Cancer. 2011;117: 4834–4845. [PubMed: 21480205]
5. Huang D, Su S, Cui X, et al. Nerve fibers in breast cancer tissues indicate aggressive tumor progression. Medicine (Baltimore). 2014;93: e172. [PubMed: 25501061]
6. Shao JX, Wang B, Yao YN, Pan ZJ, Shen Q, Zhou JY. Autonomic nervous infiltration positively correlates with pathological risk grading and poor prognosis in patients with lung adenocarcinoma. Thorac Cancer. 2016;7: 588–598. [PubMed: 27766778]
7. Madeo M, Colbert PL, Vermeer DW, et al. Cancer exosomes induce tumor innervation. Nat Commun. 2018;9: 4284. [PubMed: 30327461]
8. Lucido CT, Wynja E, Madeo M, et al. Innervation of cervical carcinoma is mediated by cancer-derived exosomes. Gynecol Oncol. 2019;154: 228–235. [PubMed: 31003747]
9. Amit M, Takahashi H, Dragomir MP, et al. Loss of p53 drives neuron reprogramming in head and neck cancer. Nature. 2020;578: 449–454. [PubMed: 32051587]
10. Shurin GV, Kruglov O, Ding F, et al. Melanoma-Induced Reprogramming of Schwann Cell Signaling Aids Tumor Growth. Cancer Res. 2019;79: 2736–2747. [PubMed: 30914431]
11. Zhao CM, Hayakawa Y, Kodama Y, et al. Denervation suppresses gastric tumorigenesis. Sci Transl Med. 2014;6: 250ra115.
12. Saloman JL, Albers KM, Li D, et al. Ablation of sensory neurons in a genetic model of pancreatic ductal adenocarcinoma slows initiation and progression of cancer. Proc Natl Acad Sci U S A. 2016;113: 3078–3083. [PubMed: 26929329]
13. Erin N Role of sensory neurons, neuroimmune pathways, and transient receptor potential vanilloid 1 (TRPV1) channels in a murine model of breast cancer metastasis. Cancer Immunol Immunother. 2020;69: 307–314. [PubMed: 31912230]
14. Prazeres P, Leonel C, Silva WN, et al. Ablation of sensory nerves favours melanoma progression. J Cell Mol Med. 2020;24: 9574–9589. [PubMed: 32691511]
15. Peterson SC, Eberl M, Vagnozzi AN, et al. Basal cell carcinoma preferentially arises from stem cells within hair follicle and mechanosensory niches. Cell Stem Cell. 2015;16: 400–412. [PubMed: 25842978]
16. Keskinov AA, Tapias V, Watkins SC, Ma Y, Shurin MR, Shurin GV. Impact of the Sensory Neurons on Melanoma Growth In Vivo. PLoS One. 2016;11: e0156095. [PubMed: 27227315]
17. Eddy K, Shah R, Chen S. Decoding Melanoma Development and Progression: Identification of Therapeutic Vulnerabilities. Front Oncol. 2020;10: 626129. [PubMed: 33614507]
18. Maibach F, Sadozai H, Seyed Jafari SM, Hunger RE, Schenk M. Tumor-Infiltrating Lymphocytes and Their Prognostic Value in Cutaneous Melanoma. Front Immunol. 2020;11: 2105. [PubMed: 33013886]
19. Bunimovich YL, Keskinov AA, Shurin GV, Shurin MR. Schwann cells: a new player in the tumor microenvironment. Cancer Immunol Immunother. 2017;66: 959–968. [PubMed: 27885383]
20. Martyn GV, Shurin GV, Keskinov AA, Bunimovich YL, Shurin MR. Schwann cells shape the neuro-immune environs and control cancer progression. Cancer Immunol Immunother. 2019.
21. Zhang SH, Shurin GV, Khosravi H, et al. Immunomodulation by Schwann cells in disease. Cancer Immunol Immunother. 2020;69: 245–253. [PubMed: 31676924]

22. Cabrita R, Lauss M, Sanna A, et al. Tertiary lymphoid structures improve immunotherapy and survival in melanoma. Nature. 2020;577: 561–565. [PubMed: 31942071]
23. Helmink BA, Reddy SM, Gao J, et al. B cells and tertiary lymphoid structures promote immunotherapy response. Nature. 2020;577: 549–555. [PubMed: 31942075]
24. Siebenhaar F, Magerl M, Peters EM, Hendrix S, Metz M, Maurer M. Mast cell-driven skin inflammation is impaired in the absence of sensory nerves. J Allergy Clin Immunol. 2008;121: 955–961. [PubMed: 18158175]
25. Karai L, Brown DC, Mannes AJ, et al. Deletion of vanilloid receptor 1-expressing primary afferent neurons for pain control. J Clin Invest. 2004;113: 1344–1352. [PubMed: 15124026]
26. Jung SR, Suprunenko T, Ashhurst TM, King NJC, Hofer MJ. Collateral Damage: What Effect Does Anti-CD4 and Anti-CD8alpha Antibody-Mediated Depletion Have on Leukocyte Populations? J Immunol. 2018;201: 2176–2186. [PubMed: 30143586]
27. Li B, Dewey CN. RSEM: accurate transcript quantification from RNA-Seq data with or without a reference genome. BMC Bioinformatics. 2011;12: 323. [PubMed: 21816040]
28. Love MI, Huber W, Anders S. Moderated estimation of fold change and dispersion for RNA-seq data with DESeq2. Genome Biol. 2014;15: 550. [PubMed: 25516281]
29. Carlson CS, Emerson RO, Sherwood AM, et al. Using synthetic templates to design an unbiased multiplex PCR assay. Nat Commun. 2013;4: 2680. [PubMed: 24157944]
30. Robins HS, Campregher PV, Srivastava SK, et al. Comprehensive assessment of T-cell receptor beta-chain diversity in alphabeta T cells. Blood. 2009;114: 4099–4107. [PubMed: 19706884]
31. Leone DP, Genoud S, Atanasoski S, et al. Tamoxifen-inducible glia-specific Cre mice for somatic mutagenesis in oligodendrocytes and Schwann cells. Mol Cell Neurosci. 2003;22: 430–440. [PubMed: 12727441]
32. Gomez-Sanchez JA, Pilch KS, van der Lans M, et al. After Nerve Injury, Lineage Tracing Shows That Myelin and Remak Schwann Cells Elongate Extensively and Branch to Form Repair Schwann Cells, Which Shorten Radically on Remyelination. J Neurosci. 2017;37: 9086–9099. [PubMed: 28904214]
33. Parfejevs V, Debbache J, Shakhova O, et al. Injury-activated glial cells promote wound healing of the adult skin in mice. Nat Commun. 2018;9: 236. [PubMed: 29339718]
34. Jiang W, He Y, He W, et al. Exhausted CD8+T Cells in the Tumor Immune Microenvironment: New Pathways to Therapy. Front Immunol. 2020;11: 622509. [PubMed: 33633741]
35. Shevchenko I, Mathes A, Groth C, et al. Enhanced expression of CD39 and CD73 on T cells in the regulation of anti-tumor immune responses. Oncoimmunology. 2020;9: 1744946.
36. Stranford S, Ruddle NH. Follicular dendritic cells, conduits, lymphatic vessels, and high endothelial venules in tertiary lymphoid organs: Parallels with lymph node stroma. Front Immunol. 2012;3: 350. [PubMed: 23230435]
37. Martinet L, Garrido I, Filleron T, et al. Human solid tumors contain high endothelial venules: association with T- and B-lymphocyte infiltration and favorable prognosis in breast cancer. Cancer Res. 2011;71: 5678–5687. [PubMed: 21846823]
38. Messina JL, Fenstermacher DA, Eschrich S, et al. 12-Chemokine gene signature identifies lymph node-like structures in melanoma: potential for patient selection for immunotherapy? Sci Rep. 2012;2: 765. [PubMed: 23097687]
39. Vella G, Guelfi S, Bergers G. High Endothelial Venules: A Vascular Perspective on Tertiary Lymphoid Structures in Cancer. Front Immunol. 2021;12: 736670. [PubMed: 34484246]
40. Heij LR, Tan X, Kather JN, et al. Nerve Fibers in the Tumor Microenvironment Are Co-Localized with Lymphoid Aggregates in Pancreatic Cancer. J Clin Med. 2021;10.
41. Zhu G, Falahat R, Wang K, Mailloux A, Artzi N, Mule JJ. Tumor-Associated Tertiary Lymphoid Structures: Gene-Expression Profiling and Their Bioengineering. Front Immunol. 2017;8: 767. [PubMed: 28713385]
42. Blanchard L, Girard JP. High endothelial venules (HEVs) in immunity, inflammation and cancer. Angiogenesis. 2021;24: 719–753. [PubMed: 33956259]
43. Ruffin AT, Cillo AR, Tabib T, et al. B cell signatures and tertiary lymphoid structures contribute to outcome in head and neck squamous cell carcinoma. Nat Commun. 2021;12: 3349. [PubMed: 34099645]

44. Goc J, Fridman WH, Sautes-Fridman C, Dieu-Nosjean MC. Characteristics of tertiary lymphoid structures in primary cancers. Oncoimmunology. 2013;2: e26836. [PubMed: 24498556]
45. Veerman K, Tardiveau C, Martins F, Coudert J, Girard JP. Single-Cell Analysis Reveals Heterogeneity of High Endothelial Venules and Different Regulation of Genes Controlling Lymphocyte Entry to Lymph Nodes. Cell Rep. 2019;26: 3116–3131 e3115. [PubMed: 30865898]
46. Ager A High Endothelial Venules and Other Blood Vessels: Critical Regulators of Lymphoid Organ Development and Function. Front Immunol. 2017;8: 45. [PubMed: 28217126]
47. Girard JP, Moussion C, Forster R. HEVs, lymphatics and homeostatic immune cell trafficking in lymph nodes. Nat Rev Immunol. 2012;12: 762–773. [PubMed: 23018291]
48. Peske JD, Thompson ED, Gemta L, Baylis RA, Fu YX, Engelhard VH. Effector lymphocyte-induced lymph node-like vasculature enables naive T-cell entry into tumours and enhanced anti-tumour immunity. Nat Commun. 2015;6: 7114. [PubMed: 25968334]
49. Schrama D, thor Straten P, Fischer WH, et al. Targeting of lymphotoxin-alpha to the tumor elicits an efficient immune response associated with induction of peripheral lymphoid-like tissue. Immunity. 2001;14: 111–121. [PubMed: 11239444]
50. Zhu W, Germain C, Liu Z, et al. A high density of tertiary lymphoid structure B cells in lung tumors is associated with increased CD4(+) T cell receptor repertoire clonality. Oncoimmunology. 2015;4: e1051922. [PubMed: 26587322]
51. Chelvanambi M, Fecek RJ, Taylor JL, Storkus WJ. STING agonist-based treatment promotes vascular normalization and tertiary lymphoid structure formation in the therapeutic melanoma microenvironment. J Immunother Cancer. 2021;9.
52. Yamakoshi Y, Tanaka H, Sakimura C, et al. Immunological potential of tertiary lymphoid structures surrounding the primary tumor in gastric cancer. Int J Oncol. 2020;57: 171–182. [PubMed: 32319601]
53. Huang S, Ziegler CGK, Austin J, et al. Lymph nodes are innervated by a unique population of sensory neurons with immunomodulatory potential. Cell. 2021;184: 441–459 e425. [PubMed: 33333021]
54. Rostock C, Schrenk-Siemens K, Pohle J, Siemens J. Human vs. Mouse Nociceptors - Similarities and Differences. Neuroscience. 2018;387: 13–27. [PubMed: 29229553]
55. Ray P, Torck A, Quigley L, et al. Comparative transcriptome profiling of the human and mouse dorsal root ganglia: an RNA-seq-based resource for pain and sensory neuroscience research. Pain. 2018;159: 1325–1345. [PubMed: 29561359]
56. Diener J, Sommer L. Reemergence of neural crest stem cell-like states in melanoma during disease progression and treatment. Stem Cells Transl Med. 2021;10: 522–533. [PubMed: 33258291]
57. Gale JR, Gedeon JY, Donnelly CJ, Gold MS. Local translation in primary afferents and its contribution to pain. Pain. 2022.
58. Monje PV, Sant D, Wang G. Phenotypic and Functional Characteristics of Human Schwann Cells as Revealed by Cell-Based Assays and RNA-SEQ. Mol Neurobiol. 2018;55: 6637–6660. [PubMed: 29327207]
59. Olivier BJ, Cailotto C, van der Vliet J, et al. Vagal innervation is required for the formation of tertiary lymphoid tissue in colitis. Eur J Immunol. 2016;46: 2467–2480. [PubMed: 27457277]
60. Chen CS, Weber J, Holtkamp SJ, et al. Loss of direct adrenergic innervation after peripheral nerve injury causes lymph node expansion through IFN-gamma. J Exp Med. 2021;218.
61. Leinwand J, Miller G. Regulation and modulation of antitumor immunity in pancreatic cancer. Nat Immunol. 2020;21: 1152–1159. [PubMed: 32807942]
62. Johansson-Percival A, He B, Li ZJ, et al. De novo induction of intratumoral lymphoid structures and vessel normalization enhances immunotherapy in resistant tumors. Nat Immunol. 2017;18: 1207–1217. [PubMed: 28892469]
63. Moussion C, Girard JP. Dendritic cells control lymphocyte entry to lymph nodes through high endothelial venules. Nature. 2011;479: 542–546. [PubMed: 22080953]
64. Colbeck EJ, Jones E, Hindley JP, et al. Treg Depletion Licenses T Cell-Driven HEV Neogenesis and Promotes Tumor Destruction. Cancer Immunol Res. 2017;5: 1005–1015. [PubMed: 28947544]

65. Faget J, Groeneveld S, Boivin G, et al. Neutrophils and Snail Orchestrate the Establishment of a Pro-tumor Microenvironment in Lung Cancer. Cell Rep. 2017;21: 3190–3204. [PubMed: 29241546]

66. Abdo H, Calvo-Enrique L, Lopez JM, et al. Specialized cutaneous Schwann cells initiate pain sensation. Science. 2019;365: 695–699. [PubMed: 31416963]

67. Varey AHR, Goumas C, Hong AM, et al. Neurotropic melanoma: an analysis of the clinicopathological features, management strategies and survival outcomes for 671 patients treated at a tertiary referral center. Mod Pathol. 2017;30: 1538–1550. [PubMed: 28731051]

68. Esteban F, Munoz M, Gonzalez-Moles MA, Rosso M. A role for substance P in cancer promotion and progression: a mechanism to counteract intracellular death signals following oncogene activation or DNA damage. Cancer Metastasis Rev. 2006;25: 137–145. [PubMed: 16680578]

69. Munoz M, Covenas R. The Neurokinin-1 Receptor Antagonist Aprepitant: An Intelligent Bullet against Cancer? Cancers (Basel). 2020;12.

70. Bujak JK, Kosmala D, Szopa IM, Majchrzak K, Bednarczyk P. Inflammation, Cancer and Immunity-Implication of TRPV1 Channel. Front Oncol. 2019;9: 1087. [PubMed: 31681615]

71. Mittal SO, Jabbari B. Botulinum Neurotoxins and Cancer-A Review of the Literature. Toxins (Basel). 2020;12.

72. Rotte A Combination of CTLA-4 and PD-1 blockers for treatment of cancer. J Exp Clin Cancer Res. 2019;38: 255. [PubMed: 31196207]

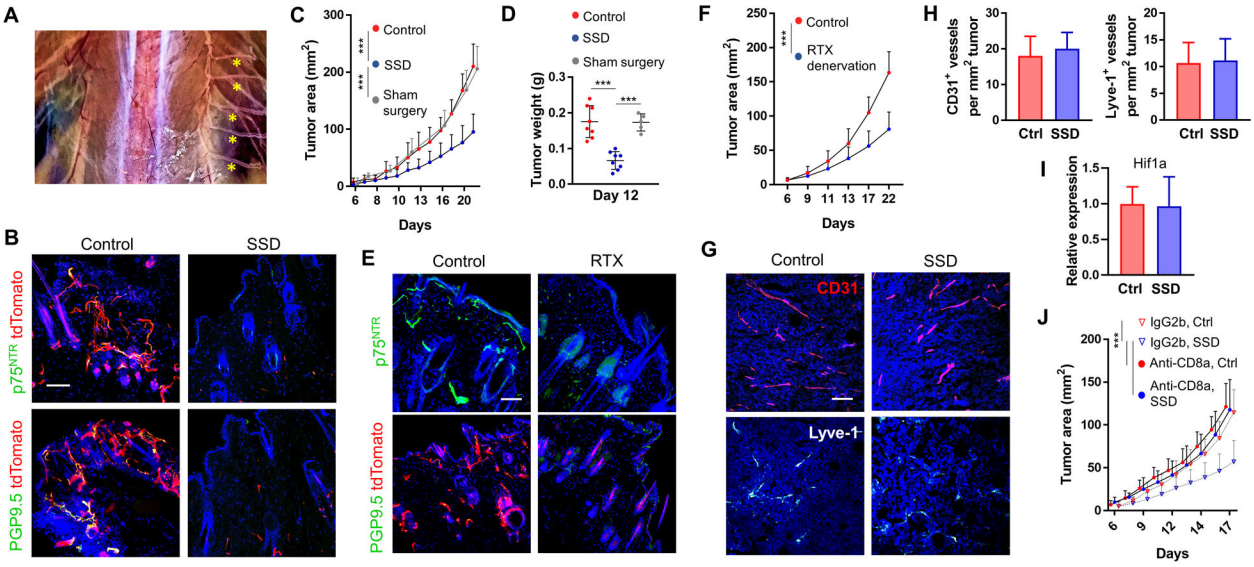

Figure 1. Sensory skin denervation results in slowed melanoma growth.

(A) Unilateral absence of dorsal thoracic sensory nerves (left side) 1 month after surgical sensory denervation (SSD) and intact nerves on the contralateral right side (yellow asterisks). (B) IF of control innervated and denervated skin (2 months after SSD) isolated from Plp1-CreERT/tdTomato$^{fl/fl}$ mice and co-stained for either PGP9.5 or p75^{NTR}. (C, D) B16F10 melanoma cells were injected into the skin of C57BL/6 mice 2 months after SSD, sham surgery, or into untreated age-matched controls. Tumor areas (C), n=15 mice, and tumor weights (D) were measured. (E) IF of the skin of C57Bl/6 mice (top row, stained for p75^{NTR}) and Plp1-CreERT/tdTomato$^{fl/fl}$ mice (bottom row, stained for PGP9.5) 1 month after i.p. RTX injections. (F) B16F10 melanoma cells were injected into the skin of C57Bl/6 mice 2 months after RTX denervation or into untreated age-matched controls. Tumor areas were measured, n=10 mice. (G) IF and (H) enumeration of CD31^{+} and Lyve-1^{+} vessels in 20-day-old B16F10 tumors isolated from control vs. SSD-treated C57BL/6 mice; n=10 tumors. (I) Expression of *Hif1a* in control vs. SSD B16F10 tumors 20 days after inoculation; n=10 tumors × 3 replicates/tumor. (J) Control and SSD-treated C57BL/6 mice were injected i.p. with anti-CD8a or IgG2b isotype control antibodies on days 0, 3, 6, 9 after B16F10 cell injection. Tumor areas were measured over time; n=10 mice. Data are mean±SD, two-way (C, F, J) or one-way (D) ANOVA with Tukey's multiple comparisons test; two-sided student's t-test (H, I). *P<0.05, **P<0.01, ***P<0.001. DAPI: blue. Scale bars, 100 μm.

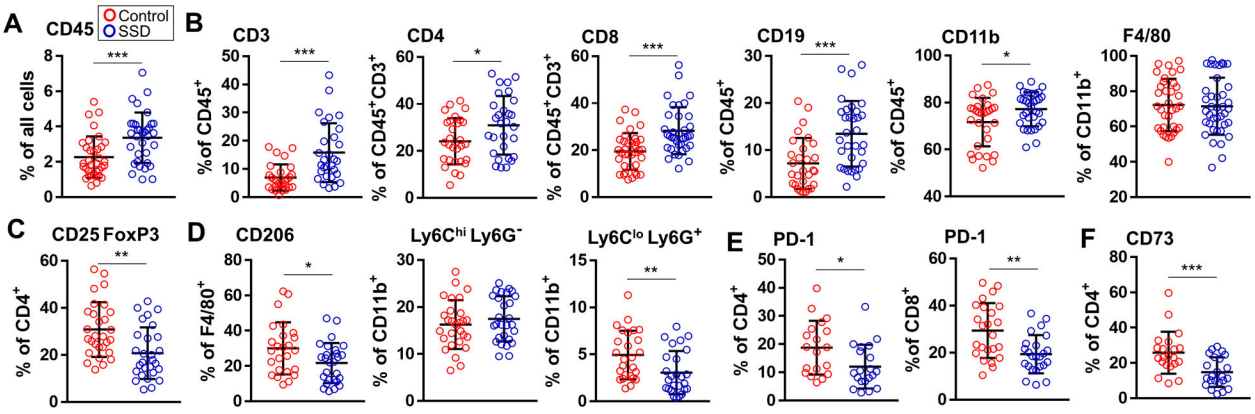

Figure 2. Sensory denervation influences the composition of tumor-infiltrating leukocytes.

Flow cytometry analyses of B16F10 tumor-infiltrating leukocytes from control C57BL/6 mice and mice after SSD. The following cells as percentages of indicated populations are shown: (A) $CD45^+$ leukocytes, (B) $CD45^+CD3^+$, $CD45^+CD3^+CD4^+$, $CD45^+CD3^+CD8^+$, $CD45^+CD19^+$, $CD45^+CD11b^+$, $CD45^+CD11b^+F4/80^+$ cells, (C) $CD45^+CD3^+CD4^+CD25^+FoxP3^+$ T_{reg}, (D) $CD45^+F4/80^+CD206^+$ macrophages, $CD45^+CD11b^+Ly6C^{hi}Ly6G^-$ and $Ly6C^{lo}Ly6G^+$ MDSCs, (E) $CD4^+PD\text{-}1^+$, $CD8^+PD\text{-}1^+$ T cells, and (F) $CD45^+CD3^+CD4^+CD73^+$ cells. Data are mean±SD, two-sided student's t-test. *P<0.05, **P<0.01, ***P<0.001; n=24–30 tumors.

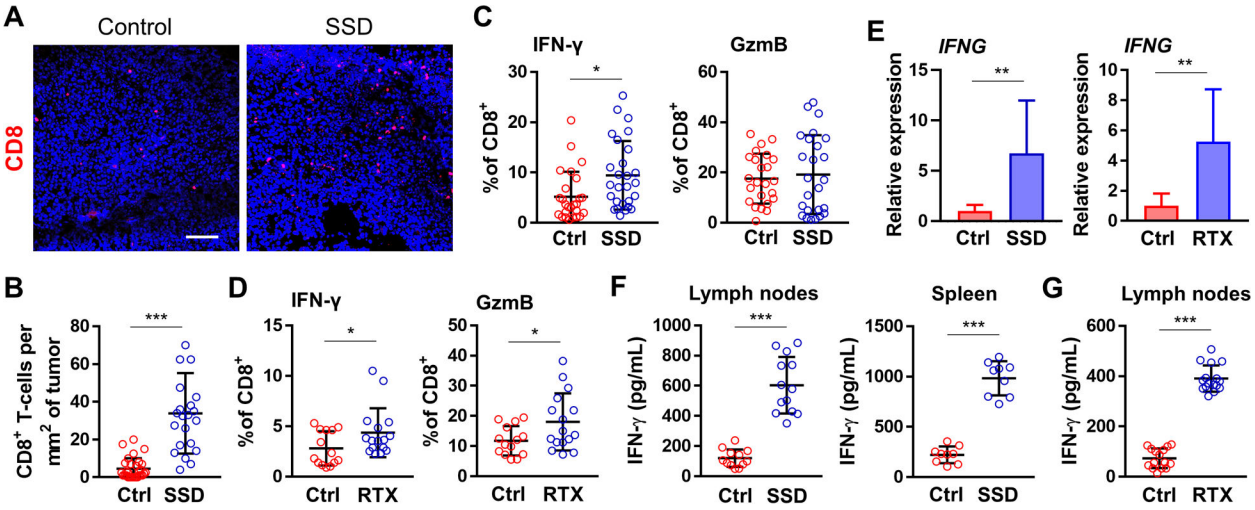

Figure 3. Sensory denervation enforces inflammatory T effector cells in the TME.

(A) IF of B16F10 tumors from control and SSD-treated C57BL/6 mice. DAPI: blue. Scale bar, 100 μm. (B) Enumeration of $CD8^+$ TILs from IF in A; n=5 tumors. (C) Flow cytometry analyses of $CD45^+CD3^+CD8^+IFN\gamma^+$ (left) and $CD45^+CD3^+CD8^+GzmB^+$ (right) cells isolated from melanoma tumors of untreated (ctrl) mice and SSD-treated mice. Data presented as a percentage of $CD45^+CD3^+CD8^+$ population; n=26. (D) Flow cytometry analyses of $CD45^+CD3^+CD8^+IFN\gamma^+$ (left) and $CD45^+CD3^+CD8^+GzmB^+$ (right) cells from melanoma tumors isolated from untreated (ctrl) C57BL/6 mice and RTX-treated mice. Data presented as a percentage of $CD45^+CD3^+CD8^+$ population; n=17. (E) Expression of *Ifng* in tumors isolated from SSD-treated (left) and RTX-treated (right) mice vs. controls; n=8 tumors × 3 replicates/tumor. (F) IFNγ ELISAs from single-cell suspensions of inguinal lymph nodes (left, n=13) and spleens (right, n=9) from B16F10-bearing control vs. SSD-treated mice. Cells were primed/restimulated with B16F10 cells *in vitro* as described in Materials and Methods. (G) IFNγ ELISAs from single-cell suspensions of inguinal lymph nodes isolated from B16F10-bearing control vs. RTX-treated mice; n=17. Data are mea±SD, two-sided student's t-test. *P<0.05, **P<0.01, ***P<0.001.

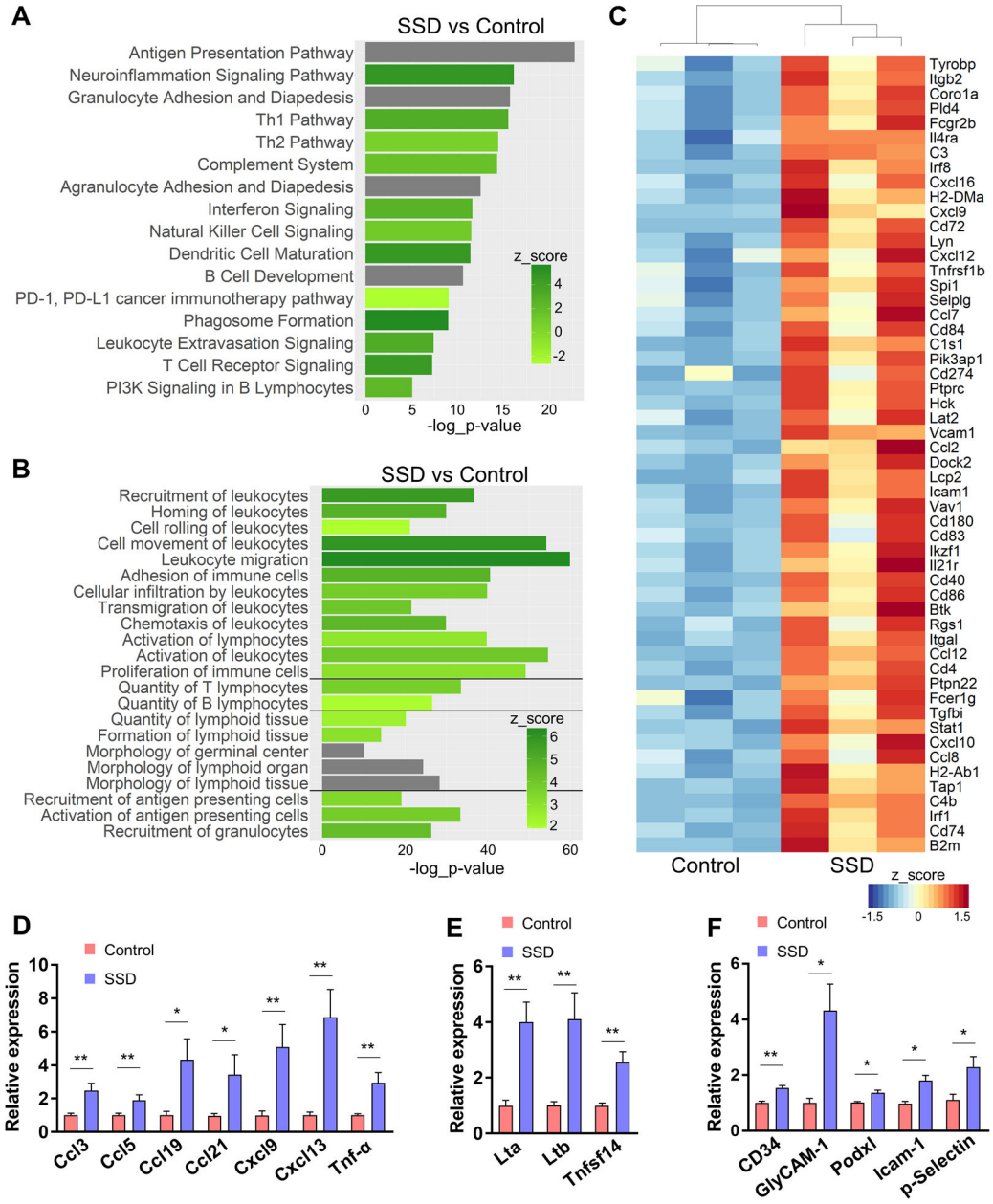

Figure 4. Sensory denervation promotes HEV maturation and TLS formation in the TME.

(A, B) Pathway analyses of differentially expressed genes in control vs. denervated B16F10 tumors in C57BL/6 mice; n=3. Selected top canonical pathways (A) and top enriched physiological pathways (B) from IPA. For each pathway, z-score and $-\log_{10}$(p-value) are indicated, unless z-score could not be determined (grey bars). (C) Heat map of an *ad hoc* panel of TLS-associated genes selected from RNA-seq analyses. (D-F) qRT-PCR analyses of selected gene products of B16F10 tumors from control vs. SSD-treated C57BL/6 mice, including TLS/HEV-related homeostatic chemokines (D), lymphotoxin receptor agonists (E), HEV-specific sialylated mucin-like glycoproteins and other leukocyte homing receptors (F); n=10 tumors × 3 replicates/tumor. Data are mean±SEM, two-sided student's t-test. *P<0.05, **P<0.01.

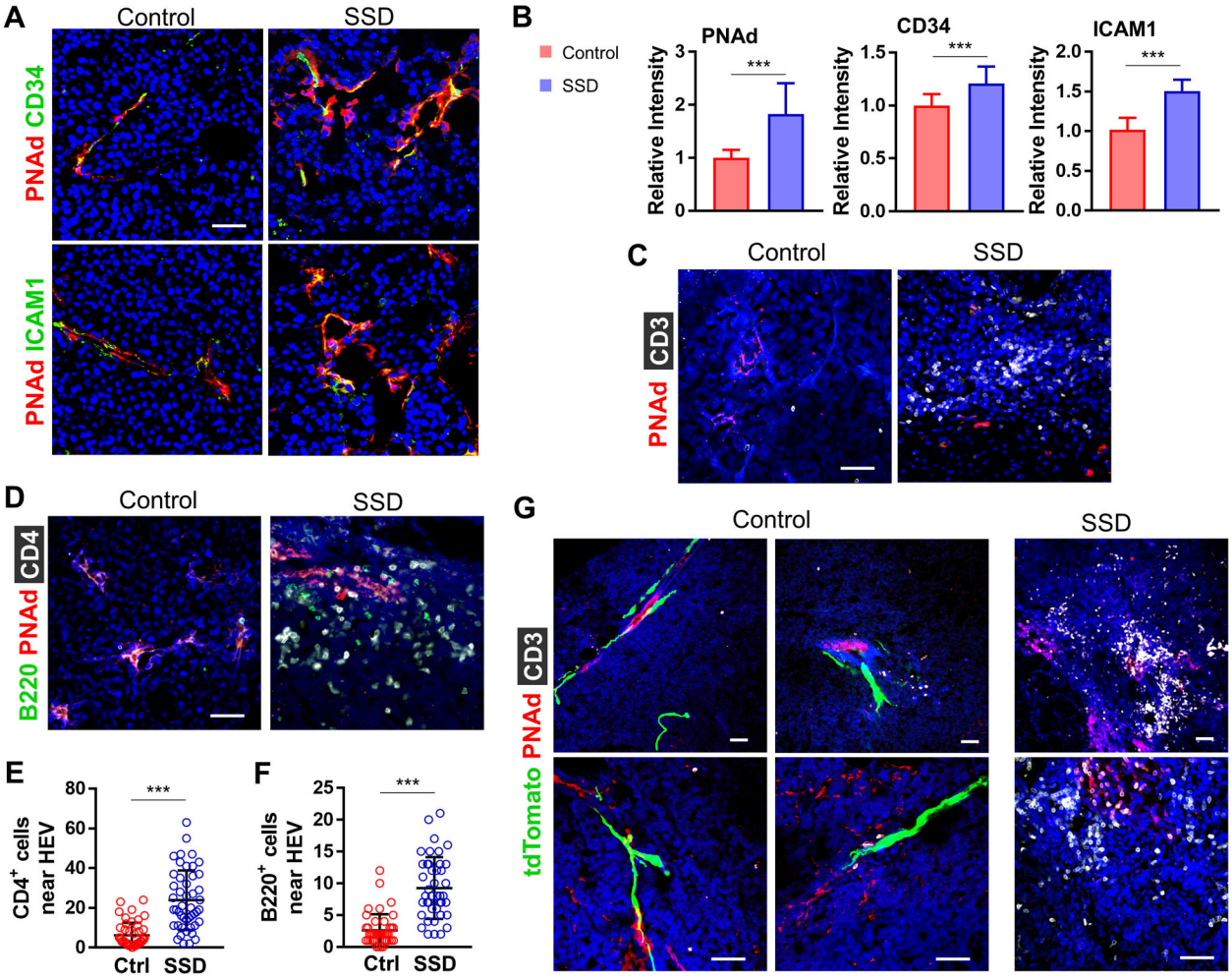

Figure 5. Sensory neurons prevent lymphocyte infiltration and formation of TLS-like structures.

(A) IF of B16F10 tumors isolated from control vs. SSD-treated C57BL/6 mice for $PNAD^{+}CD34^{+}ICAM11^{+}$ HEVs. (B) Tumor PNAd, CD34, and ICAM1 relative fluorescence intensities over 10^5 μm^2 visual field; n=5 tumors × 3 replicates/tumor. IF of tumors from control vs. SSD-treated C57BL/6 mice: (C) $CD3^{+}$ lymphocytes adjacent to $PNAd^{+}$ HEVs, (D) $CD4^{+}$ T cells and $B220^{+}$ B cells adjacent to $PNAd^{+}$ HEVs. Enumeration of (E) $CD4^{+}$ T cells and (F) $B220^{+}$ B cells adjacent to $PNAd^{+}$ HEVs in tumors from control vs. SSD-treated C57BL/6 mice; n=10 tumors. (G) IF of tumors from control vs. SSD-treated Plp1-CreERT/tdTomato$^{fl/fl}$ mice. Data represent mean±SD, two-sided student's t-test. *P<0.05, **P<0.01, ***P<0.001. DAPI: blue. Scale bars, 50 μm.

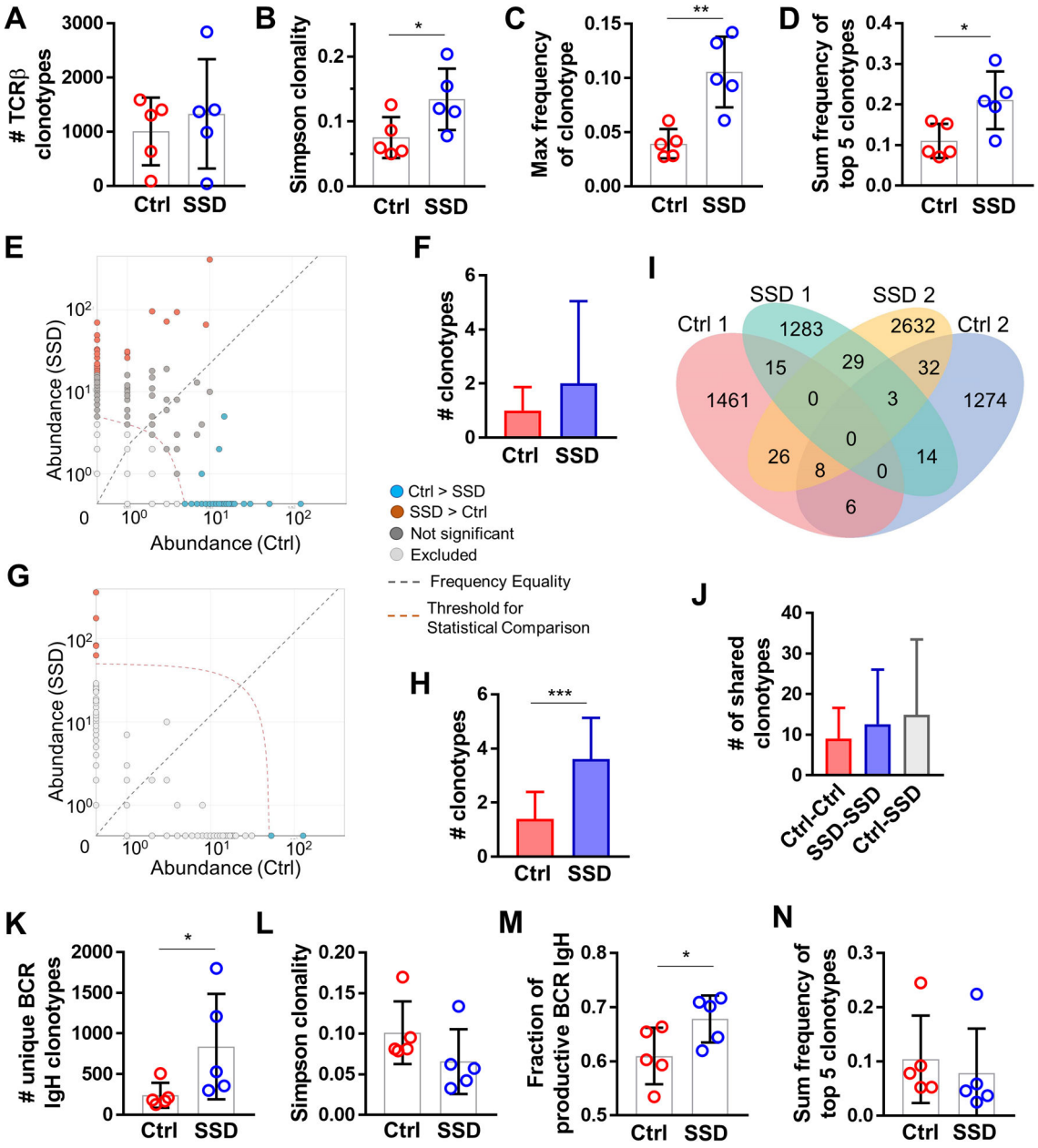

Figure 6. Sensory neurons modulate T-cell and B-cell repertoires in the TME.

TCRβ CDR3 immuno-sequencing of B16F10 tumors from control vs. SSD-treated C57BL/6 mice; n=5 tumors per group. (A) Total number of productive unique TCRβ clonotypes per tumor. (B) Simpson clonality of TCRβ clonotypes per tumor. (C) Frequency of the most abundant TCRβ clonotype per tumor. (D) Sum of frequencies of top 5 most abundant TCRβ clonotypes per tumor. (E) Representative pairwise differential abundance plot demonstrating shared TCRβ clonotypes with > 5 abundance (above the indicated threshold) and significantly higher frequency in either control (blue) or SSD (brown) group. (F) Pairwise analysis of control vs SSD groups as in E, demonstrating shared TCRβ clonotypes between control and SSD groups with > 5 abundance, and significantly overrepresented in either group. (G) Representative pairwise differential abundance plot demonstrating unique

clonotypes with > 50 abundance (above the indicated threshold) in either control (blue) or SSD (brown) group. (H) Pairwise analysis of control vs SSD groups as in G, demonstrating unique TCRβ clonotypes in control or SSD group with > 50 abundance. (I) Representative Venn diagram of unique and shared TCRβ clonotypes in two of five tumors from control and SSD groups. (J) Number of shared TCRβ clonotypes from inter- and intra-group pairwise analyses. (K-N) BCR IgH CDR3 immuno-sequencing of B16F10 tumors from control vs. SSD-treated C57Bl/6 mice; n=5 tumors per group. (K) Total number of productive unique BCR IgH clonotypes per tumor. (L) Simpson clonality of BCR IgH clonotypes per tumor. (M) Fraction of productive BCR IgH clonotypes of total clonotypes per tumors. (N) Sum of frequencies of top 5 most abundant BCR IgH clonotypes per tumor. Data are means±SD, two-sided student's t-test. *P<0.05, **P<0.01, ***P<0.001.

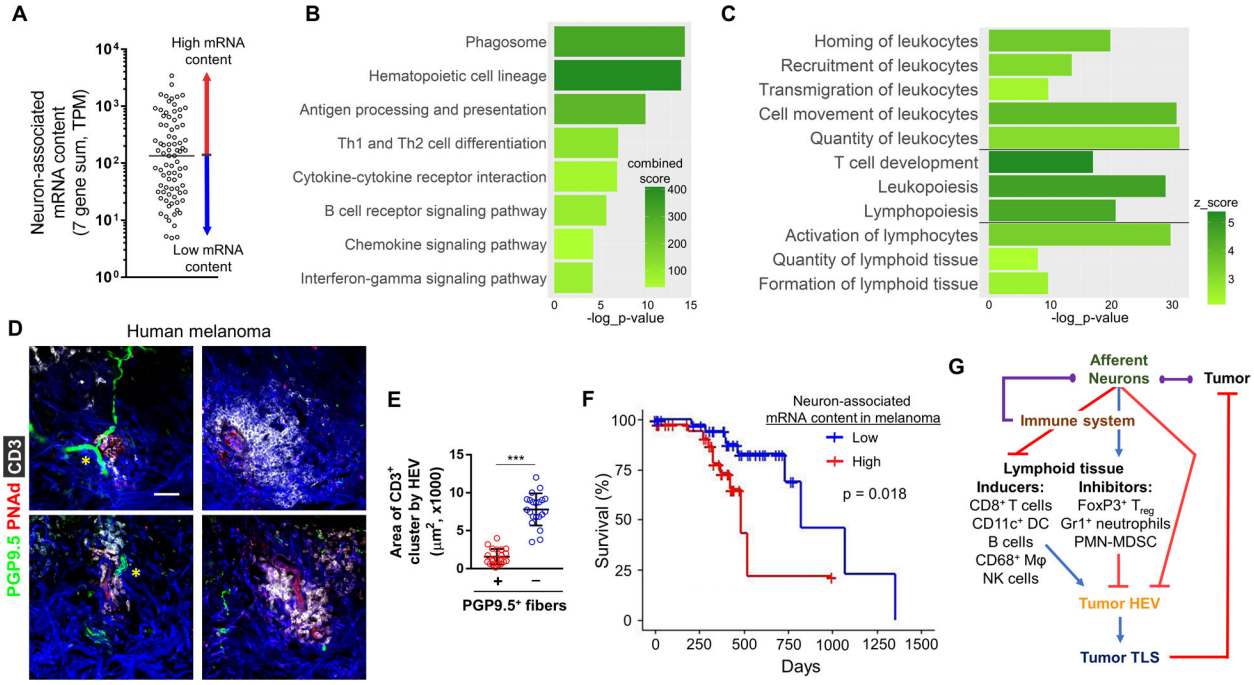

Figure 7. Neuron-associated mRNA content in human melanomas negatively correlates with TLS formation, tumor immunity, and overall survival.

(A) Patients with melanoma were divided into two groups, high (red) and low (blue) neuron-associated mRNA (NAmRNA), based on the sum of transcripts per million (TPM) of seven genes highly expressed in sensory neurons. Pathway analyses of DEGs upregulated in low NAmRNA group vs high NAmRNA group were performed. (B) Select top enriched pathways from Enrichr and (C) select physiological pathways from IPA. For each pathway, z-score or combined-score and $-\log_{10}$(p-value) are indicated. (D) Representative IF of human primary cutaneous melanomas, showing small $CD3^+$ (white) cellular clusters around $PNAd^+$ HEVs (red) and $PGP9.5^+$ (green) neurons (yellow asterisks) and larger $CD3^+$ clusters around $PNAd^+$ HEVs not associated with neurons (right column). DAPI: blue. Scale bar, 50 µm. (E) Areas of intratumoral $CD3^+$ cell clusters around $PNAd^+$ HEVs with or without associated $PGP9.5^+$ fibers; n=21 (7 clusters × 3 human melanomas). (F) Kaplan-Meier survival plot for melanoma patient cohort sub-divided into high (red) and low (blue) NAmRNA groups. Vertical lines represent days to last follow-up of alive patients. (G) Schematic of the proposed neuroimmune regulatory mechanism of TLS formation in the melanoma TME. Afferent neurons may hinder tumoral HEV maturation (and TLS formation) directly and/or indirectly by promoting influx of lymphoid tissue-inhibiting regulatory immune cells, while suppressing trafficking, expansion, and activation of lymphoid tissue-inducing immune cells. Poor TLS formation promotes tumor progression and decreases overall survival. The regulatory network may include immune cells' impact on the neurons and a direct tumor-nerve interaction (purple lines). Data are means±SD, two-sided student's t-test. *P<0.05, **P<0.01, ***P<0.001.